Study on the operating characteristics of Stirling engine based on an optimized analysis method[*]

Shangdong Yang,[1] Wenpei Feng,[1, †] Yugao Ma,[2] and Zhixing Gu[1]

[1]*College of Nuclear Technology and Automation Engineering,*
Chengdu University of Technology, Chengdu 610059, China
[2]*Science and Technology on Reactor System Design Technology Laboratory,*
Nuclear Power Institute of China, Chengdu 610213, China

The Stirling engine, as a closed-cycle power machine, possesses excellent emission characteristics and broad energy adaptability. Second-order analysis methods find extensive use during the foundational design and thermodynamic examination of Stirling engines due to their commendable model precision and remarkable efficiency. To scrutinize the effect of Stirling engine design parameters on the cyclical work output and efficiency, this paper formulates a series of differential equations for the Stirling cycle employing second-order analysis methods, subsequently augmenting the predictive accuracy by integrating considerations of loss mechanisms. Additionally, an iterative method for the convergence of average pressure is introduced. The predictive capability of the established model is validated via the GPU-3 and RE-1000 experiment data. Per the model, parameters such as the operational fluid, the porosity of the regenerator, and the diameter of the wire mesh, and their influence on the resulting work output and cyclic efficiency of the Stirling engine are analyzed, thereby facilitating a broader understanding of the engine's functional characteristics. Findings suggest that hydrogen, courtesy of its lower dynamic viscosity coefficient, can engender superior output power. The loss due to flow resistance tends to increase alongside the rotational speed. Additionally, under conditions of elevated rotational speed, the loss from flow resistance declines in cases of increased porosity, and enhancement of the porosity to diminish flow resistance losses can boost both the engine's output work and cyclic efficiency. As porosity rises further, the hydraulic diameter and the dead volume in the regenerator continue to expand, causing the pressure drop within the engine to become the dominant factor in the output power's gradual reduction. Furthermore, extending the length of the regenerator results in a decrease in output work — though the thermal cycle efficiency initially experiences an increase before eventually declining. Based on these insights, the paper pursues optimal designs for the Stirling engine.

I. INTRODUCTION

As the call for advanced extraterrestrial exploration voyages perpetually escalates, the confinement posed by solar and chemical energy sources becomes glaringly evident in cosmic frontier exploration. Nuclear energy possesses the aptitude to furnish sustained power supply, extending from the lunar to even the expanse of remote celestial bodies, thereby catering to the diverse requisites of space missions, including but not limited to the establishment of enduring outposts (Fig.1). Graced with an extended lifespan, exceptional energy quantum, and steadfast operational efficacy, the Space Nuclear Reactor Power System (SNRPS)[1] triumphs as the optimal selection for executing interstellar missions. The power prerequisites encompassing various tasks[2, 3] of cosmic exploration, such as deep space voyages, orbital space stations, and planetary surface infrastructures, within the range of 10 to 1000 kilowatts[4, 5]. For such space-bound expeditions, a power conversion system, imbued with a lengthy serviceable life, high dependability, and substantial power density,

is pivotal. The heat pipe-cooled reactor[6–11], an innovative nuclear apparatus, harnesses heat pipes to transfer the reactor's core heat directly to its secondary system. The Stirling engine, crafted by the ingenious British engineer Robert Stirling in 1816[12], heralds a plethora of benefits, encompassing adaptability with virtually all energy sources, diminished noise levels, and an indifference to pressure fluctuations. Recent years have bore witness to notable headway in the fabrication of kilowatt-scale SNRPS that amalgamates Stirling engines with heat pipe-cooled reactors[13–16]. The Stirling cycle can achieve a relatively high thermodynamic-to-electrical conversion efficiency, theoretically ranging from 20% to 40%[17]. Hence, the integration of heat pipe-cooled reactors with Stirling engines has been actively pursued as an area of research. The U.S. has harnessed the principles of the Stirling cycle in the conceptualization and design of a diverse array of kilowatt-scale heat pipe fission reactors, such as the Heat Pipe Mars Exploration Reactor (HOMER)[18] and the Kilowatt Reactor Utilizing Stirling Technology (KRUSTY, (Fig.2))[19–21]. In March 2018, KRUSTY successfully operated as a fission power system and was the first nuclear-powered operation of any truly new reactor concept in the United States in over 40 years[22]. The performance of the Stirling engine influences the thermal output of the reactor, so it is necessary to analyze its operational characteristics. The Stirling cycle thermodynamic model is widely used to describe and predict the process and thermal performance of the Stirling cycle. Ideally, the Stirling cycle consists of two isothermal processes and two constant-capacity processes, and the thermal conversion efficiency is equal to the Carnot cycle efficiency. Nonetheless, in practical terms,

Fig. 1. Space nuclear energy

Fig. 2. Nuclear fission system and thermal management system of Kilopower[34]
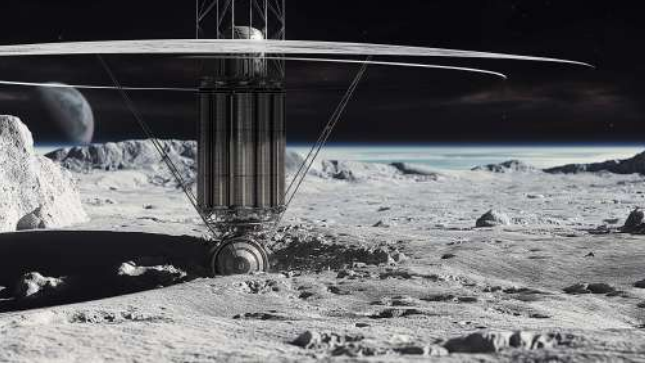
various energy dissipations demand consideration, an aspect of paramount importance in the construction of an accurate thermodynamic model.

Martini[23]classified the Stirling analytical model into zero-order, first-order, second-order, third-order and fourth-order. The zero-order analysis employs empirical relationships derived from fitting a substantial volume of experimental data, facilitating quick and straightforward calculations of the Stirling engine's power output and efficiency. This methodology, represented by the Beale number method[24], can be beneficial for the engine's qualitative examination. First-order analysis of the Stirling cycle incorporates an extensively idealized model, utilizing variables like the temperatures of the cold and hot sources, pressure, rotational velocity, piston diameter, and piston stroke. It predicts the output work and cycle efficiency of the Stirling engine based on the conservation of energy between the working spaces. Schmidt's analysis method [24] is a typical example of a first-order analysis method, where the overall engine is integrated into three spatial segments (dead space, expansion space, and compression space). Herein, the prevailing temperatures are presupposed to remain constant, often referred to as isothermal analysis. However, the exceedingly ideal nature of this analysis results in calculations that deviate significantly from real-world Stirling engines. However, the exceedingly ideal nature of this analysis results in calculations that deviate significantly from real-world Stirling engines. In contrast, the second-order Stirling analysis model elaborates on potential power losses and heat dissipations, rendering more precise results and gaining widespread usage for Stirling cycle period analyses. Nevertheless, there is still a gap between the calculation accuracy of traditional second-order analysis methods and experimental values, with an absolute error of about 30-40% in the estimation of cycle efficiency[24]. To refine prediction accuracy, numerous studies have aimed at optimizing the second-order analysis model. Sayyaadi's team combined finite speed thermodynamics with multiple losses and proposed Simple II[25] and CAFS[26] models, which reduced the error between the simulated and experimental values of cycle efficiency to about 6.1%-18.7%. Based on the ideal adiabatic model, Ni et al.[27] considered heat losses such as incomplete regeneration losses in the regenerator and power
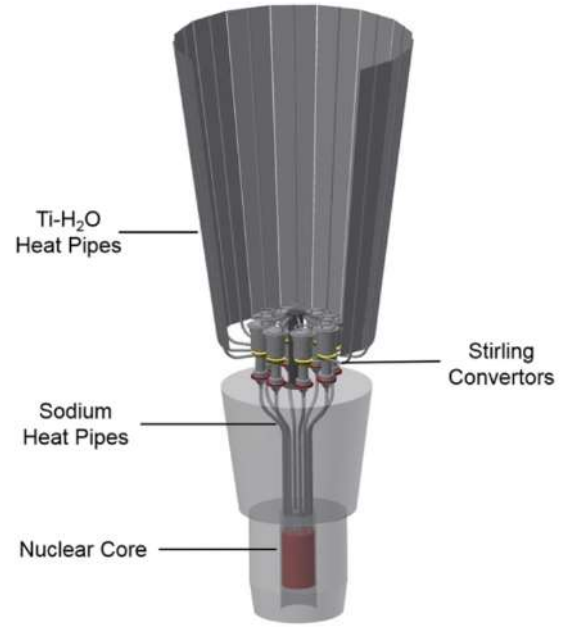
losses such as flow resistance losses and developed the ISAM model. The error between the simulated and experimental values of cycle efficiency was reduced to about 9.8%-19.9%. The third-order Stirling analysis model[28–30] divides Stirling into multiple nodes in the mainstream direction, solves the partial differential equations of mass, momentum, and energy conservation at each node to obtain heat and output power, and has higher computational accuracy. However, its calculation speed is much slower than that of the second-order model. The fourth-order analysis method, also known as the Computational Fluid Dynamics (CFD) method[31–33], has higher requirements for computing resources and is difficult to carry out system analysis. Bearing in mind the need for precision and calculation speed to facilitate the subsequent development of the thermoelectric conversion module of the heat pipe-cooled reactor system analysis code, this paper selects the second-order analysis methodology for the progression of the Stirling analysis model.

This paper proposes to refine the Simple analysis method by incorporating additional loss terms in the loss module, as seen in models such as Simple-II, CAFS, and ISAM. These additional losses include conductive heat loss, shuttle loss of the displacer piston, leakage loss, finite speed loss of the piston, and mechanical friction loss.

It is worth noting that, at present, the free-piston Stirling engine is the optimal choice for kilowatt-scale space nuclear power systems. In contrast, the application of the GPU-3 in this field appears somewhat out of place. However, most scholars and research institutions use the GPU-3, a well-known beta-type Stirling engine, as a research case for academic studies. As early as the last century, NASA conducted extensive testing on it, confirming its efficiency and reliability. Notably, Yang et al.[15] proposed a dynamic model of
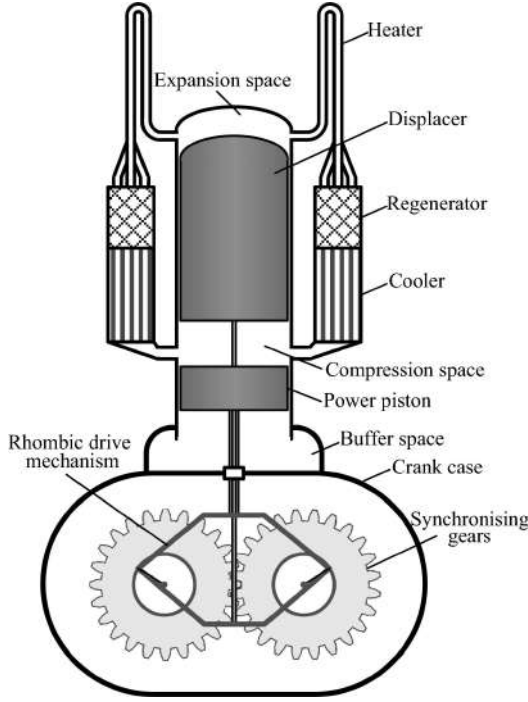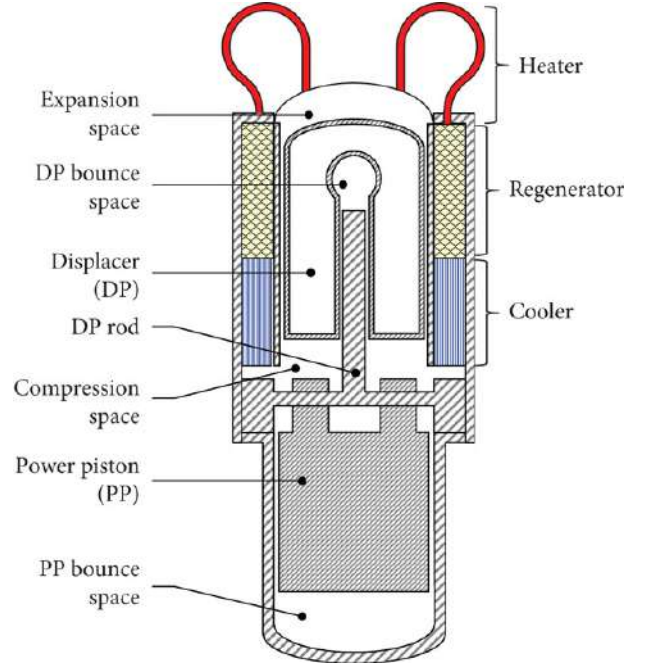
Fig. 3. GPU-3 Stiring engine

Fig. 4. RE-1000 Stiring engine

a lunar surface nuclear power system that combines a secondary Stirling cycle analysis method, using the GPU-3 Stirling device. They analyzed the transient response of the reactor under different operating conditions and various space environmental temperatures.

The accuracy of the model in this paper is validated against various second-order analysis models and experimental data from GPU-3 (Fig.3) and the free-piston Stirling engine RE-1000 (Fig.4) [35, 36] . The calculation has proven that the model is suitable for simulating both beta-type and free-piston Stirling engines. The calculation of the average pressure incorporates a pressure convergence iterative method, enabling rapid convergence of the average pressure. Based on the developed model, an appraisal of the operational characteristics indwelling the Stirling engines is undertaken. This paper proceeds to simulate Stirling cycles with usage of hydrogen and helium as working mediums under varying pressures and rotational velocities to interrogate how their distinct thermophysical properties bear upon the engine performance. Moreover, this paper probes the effect of regenerator parameters such as porosity, mesh diameter, and the axial length of the regenerator on output work and cycle efficiency at different rotational speeds and suggests optimization directions for these parameters based on the simulation outcomes. Given that the heater and cooler of a Stirling engine are in direct contact with the heat source and the cold sink, any changes in the temperatures of these sources will directly alter the temperatures of the heater and cooler, thus affecting the engine's performance. To scrutinize the consequences of temperature differentials at the hot and cold ends, Stirling cycles are simulated under various temperature ratios.

II. STIRLING MODEL

A. Adiabatic modeling

Models based on the oscillatory flow characteristics without pressure gradients are widely used for Stirling cycle characterization. The Stirling engine is divided into five chambers (shown in Fig.5), namely, expansion space, heater, regenerator, cooler, and compression space, and the second-order analysis method is based on the ideal cycle, where the mass and energy conservation equations and the gas equation of state of each chamber are solved to obtain an analytical solution, which allows further calculation of the various power losses and heat losses, and obtains the output power and the required heat that are closer to the actual situation. During the development of the ideal adiabatic model, the following assumptions were made:

(1) The working fluid is an ideal gas;

(2) There is no leakage of the working fluid in the cycle, and its mass remains constant;

(3) The temperature of the working gas in the cooler and heater is considered to be equal to the wall temperature and is held constant;

(4) The instantaneous pressure throughout the system is equal;

(5) Heat leakage between the compression space and the expansion space, as well as heat transfer to the environment, is negligible;

(6) The kinetic and potential energy of the gas flow are ignored.

The adiabatic model differential equation set is shown in Table 1, and the subscripts c, k, r, h, and e represent the com-
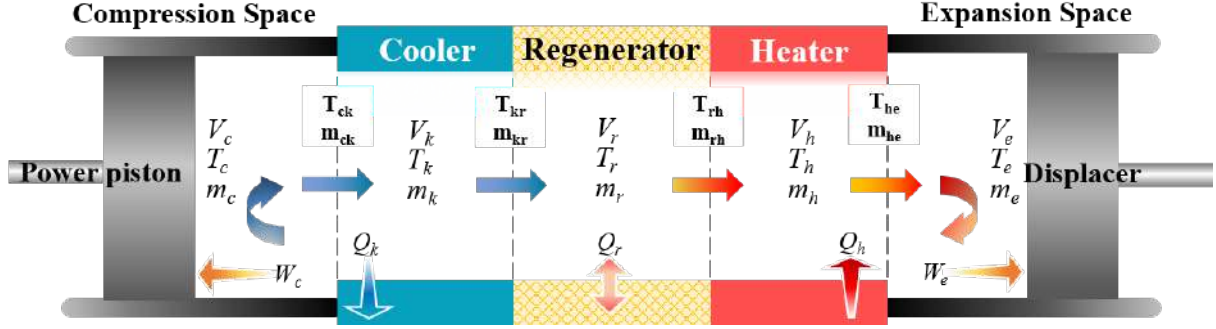
Fig. 5. The diagrammatic representation of the model in the adiabatic analysis methodology

pression cavity, cooler, return heaters, heaters, and expansion cavity, respectively. The subscripts ck, kr, rh, and he represent the four interfaces between the five components of the compression space, cooler, heat return, heater, and expansion space, respectively.

B. Modification of the Adiabatic Model

The Simple analysis method only considers the effect of non-ideal heat transfer and pressure loss in the heat exchanger. In this paper, based on the Simple analysis method, the mass leakage loss term and the distribution piston shuttle loss are coupled in the energy conservation equation.

(1)Shuttle heat loss. Shuttle loss is primarily caused by the reciprocating movement of the displacer piston between the hot and cold cylinders. There is a significant temperature gradient at both ends of the displacer piston, leading to heat loss as some of the heat is directly conducted to the cold end through the piston. The differential expression for this is:

$$dQ_{shu} = \frac{\pi S^2 k_g D_d}{8JL_d}(T_e - T_c) \quad (1)$$

where, S is the displacer stroke; k_g is the gas thermal conductivity; D_d is the displacer diameter; J is the gap between the displacer and the cylinder.

III. CALCULATION AND VALIDATION

A. Calculation process

(2)Seal leakage loss. In the actual operation of the engine, there will be a certain pressure difference between the compression space and the buffer space, which will lead to a portion of the gas through the gap between the piston and the cylinder wall in the compression space and the buffer space back and forth, resulting in leakage losses. The leakage to the buffer space was calculated as follows:

$$m_{leak} = \pi D\frac{P + P_{buffer}}{4RT_g}\left(u_p J - \frac{J^3}{6\mu}\frac{P - P_{buffer}}{L_p}\right) \quad (2)$$

Table 1. Ordinary differential equations in the Adiabatic analysis

$$p = \frac{MR}{\frac{V_c}{T_c} + \frac{V_k}{T_k} + \frac{V_r}{T_r} + \frac{V_h}{T_h} + \frac{V_e}{T_e}} \quad \text{Pressure}$$

$$dp = \frac{-\gamma p(\frac{dV_c}{T_{ck}} + \frac{dV_e}{T_{he}})}{\frac{V_c}{T_{ck}} + \gamma(\frac{V_k}{T_k} + \frac{V_r}{T_r} + \frac{V_h}{T_h}) + \frac{V_e}{T_{he}}}$$

$$m_c = pV_c/RT_c \quad \text{Mass}$$
$$m_k = pV_k/RT_k$$
$$m_r = pV_r/RT_r$$
$$m_h = pV_h/RT_h$$
$$m_e = pV_e/RT_e$$
$$dm_c = \frac{pdV_c + V_c dp/\gamma}{RT_{ck}}$$
$$dm_e = \frac{pdV_e + V_e dp/\gamma}{RT_{he}}$$
$$dm_k = m_k dp/p$$
$$dm_r = m_r dp/p$$
$$dm_h = m_h dp/p$$
$$\dot{m}_{ck} = -dm_c \quad \text{Mass flow}$$
$$\dot{m}_{kr} = \dot{m}_{ck} - dm_k$$
$$\dot{m}_{he} = -dm_e$$
$$\dot{m}_{rh} = \dot{m}_{he} + dm_h$$
$$T_{kr} = T_k$$
$$T_{rh} = T_h$$
$$if \dot{m}_{ck} > 0, T_{ck} = T_c, else T_{ck} = T_k \quad \text{Conditional}$$
$$if \dot{m}_{he} > 0, T_{he} = T_h, else T_{he} = T_e \quad \text{temperature}$$
$$dT_c = T_c(dp/p + dV_c/V_c - dm_c/m_c) \quad \text{Temperature}$$
$$dT_c = T_c(dp/p + dV_c/V_c - dm_c/m_c)$$
$$dQ_k = V_k dp C_v/R - C_p(T_{ck}\dot{m}_{ck} - T_{kr}\dot{m}_{kr}) \quad \text{Energy}$$
$$dQ_r = V_r dp C_v/R - C_p(T_{kr}\dot{m}_{kr} - T_{rh}\dot{m}_{rh})$$
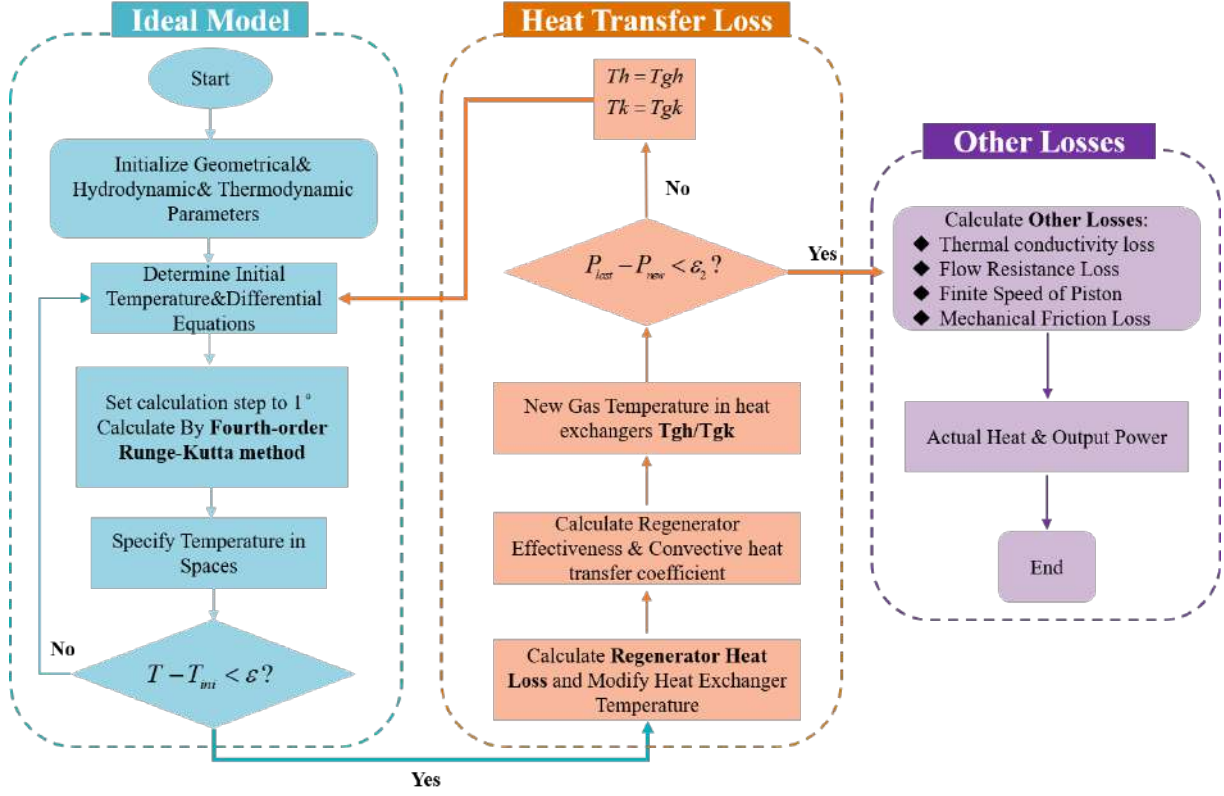$$dQ_h = V_h dp C_v/R - C_p(T_{rh}\dot{m}_{rh} - T_{he}\dot{m}_{he})$$
$$dW_c = pdV_c + pdV_e$$

Fig. 6. Calculation process

$$b_1 = \sqrt{L^2 - (e - r)^2}$$

$$b_2 = \sqrt{(L - r)^2 - e^2}$$

$$b_3 = \sqrt{L^2 - (e + r)^2}$$

$$b_\theta = \sqrt{L^2 - (e + r)^2}$$

$$V_e = V_{cle} + A_d (b_\theta - b_2 - r \sin \theta)$$

$$V_c = V_{clc} + 2 A_p (b_1 - b_\theta)$$

$$\frac{dV_c}{d\theta} = \frac{-2 A_p r \sin \theta (e + r \cos \theta)}{b_\theta}$$

$$\frac{dV_e}{d\theta} = -\frac{\left(\frac{dV_c}{d\theta}\right) A_d}{2 A_p} - A_d r \cos \theta$$
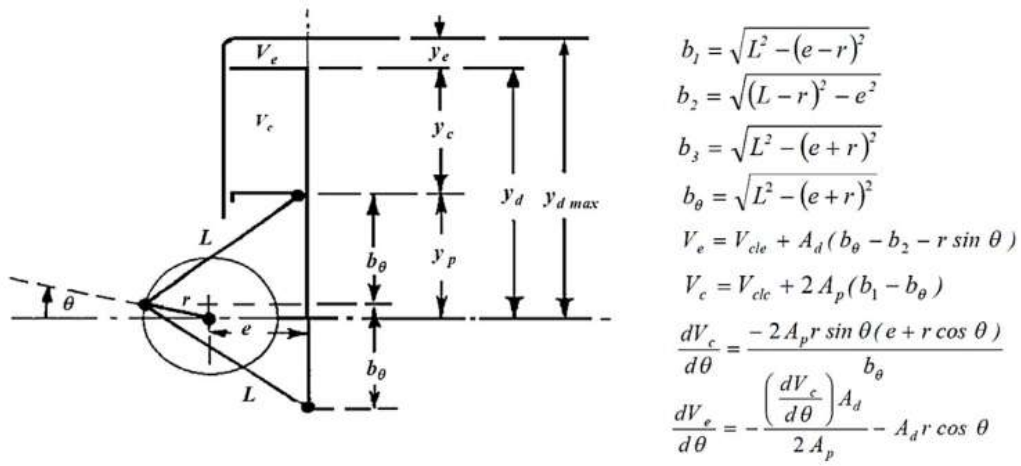
Fig. 7. The geometric relationship of the drive equation

where, P is the pressure in compression space; D is the diameter of the cylinder; P_{buffer} is the pressure of buffer space; J is the gap between piston and cylinder; L_p is the length of the piston;

Coupling the shuttle loss and leakage loss with the differential equations in the adiabatic analysis method, the pressure and pressure differential terms are changed to:

$$M = \frac{p \left(\frac{V_c}{T_c} + \frac{V_k}{T_k} + \frac{V_r}{T_r} + \frac{V_h}{T_h} + \frac{V_e}{T_e} \right)}{R} - \pi D \frac{P + P_{buffer}}{4 R T_g} \left(u_p J - \frac{J^3}{6\mu} \frac{P - P_{buffer}}{L_p} \right) \tag{3}$$

$$dp = \frac{-p(\frac{dV_c}{T_{ck}} + \frac{dV_e}{T_{he}}) + \frac{dQ_{shuttle}R}{4RT_g}\left(\frac{T_{he}-T_{ck}}{T_{he}T_{ck}}\right) + Rdm_{leak}}{\frac{V_c}{\gamma T_{ck}} + (\frac{V_k}{T_k} + \frac{V_r}{T_r} + \frac{V_h}{T_h}) + \frac{V_e}{\gamma T_{he}}} \tag{4}$$

The mass differential equation changes to:

$$dm_c = \frac{pdV_c + V_c dp/\gamma}{RT_{ck}} - \frac{dQ_{shuttle}}{c_p T_{ck}} \tag{5}$$

$$dm_e = \frac{pdV_e + V_e dp/\gamma}{RT_{he}} - \frac{dQ_{shuttle}}{c_p T_{he}} \tag{6}$$

B. Non-idea heat transfer

The heat recovery performance of a Stirling engine is evaluated by the efficiency of the regenerators. The efficiency of the regenerator is defined as the ratio of the actual enthalpy change to the maximum enthalpy change of the working fluid in the regenerators. When the gas flows from the cooler to the heater, the temperature at which it exits the return heaters will be slightly lower than the temperature of the heater. The gas will need to absorb more heat from the heater (external heat source), resulting in a less efficient heat cycle. So the actual heat absorption and heat release can be written as:

$$\begin{aligned} Q_h &= Q_{hi} + Q_{rloss} = Q_{hi} + Q_{ri}\left(1 - \varepsilon\right) \\ Q_k &= Q_{ki} - Q_{rloss} = Q_{ki} + Q_{ri}\left(1 - \varepsilon\right) \end{aligned} \tag{7}$$

where, Q_h is heat addition to the working fluid in the heater; Q_k is heat rejection to the cooler; Q_{rloss} is heat loss in the imperfect regenerator; Q_{ri} is the amount of regenerator heat transferred in ideal process and ϵ is the effectiveness of the regenerator calculated as:

$$\begin{aligned} \varepsilon &= \frac{NTU}{1 + NTU} \\ NTU &= \frac{St \cdot A_{wg}}{2A} \end{aligned} \tag{8}$$

where, NTU is the number of heat transfer units; A_{wg} internal wetted area of the regenerator; A is cross-sectional area of the regenerator and St is the Stanton number calculated as:

$$St = 0.46Re^{-0.4}Pr^{-0.1} \tag{9}$$

where, Re is the Reynolds number; Pr is the Prandtl number. In this paper; Pr is taken as a constant of 0.71. The Reynolds number in the regenerator is calculated as:

$$Re = \frac{d_m \varphi}{1 - \varphi} \tag{10}$$

where, d_m is the diameter of the regenerator wire; φ is the porosity coefficient. The heater and cooler are also non-ideal, and the actual temperature of the gases in the two heat exchangers depends on the heat losses in the return heaters and the convective heat transfer between the gases and the walls in the heater and cooler. The actual gas temperature in the heat exchanger is given as follows:

$$T_{gh} = T_{wh} - \frac{Q_{ach}}{h_h A_{wh}} \tag{11}$$

$$T_{gk} = T_{wk} - \frac{Q_{ack}}{h_k A_{wk}} \tag{12}$$

where Q_{ach} is the actual heat absorbed in the heater; Q_{ack} is the actual heat rejection of the cooler; W_{ac} is the actual indicated power output; h is the heat transfer coefficient in the heater and cooler. The heat transfer coefficient is given as follows:

$$h = \frac{f_r \mu C_p}{2dPr} \tag{13}$$

In the analysis of the Stirling engine cycle, T_{wh} and T_{wk} denote the wall temperatures of the heater and the cooler, respectively, and are generally set as constant values.

C. Other losses effects

(1)Thermal conductivity loss. The regenerator is connected to the cooler and the heater, and the heat from the hot end flows through the cylinder wall of the return heaters to the cold end, which is the main source of heat conduction loss. It can be evaluated according to the Fourier law[37]:

$$Q_w = \frac{k_m A_w \Delta T}{l} \tag{14}$$

where, k_m is the heat conduction coefficient of the material; A_w is the Thermal conductivity cross section; l is the conductivity length.

(2)Flow resistance loss. The pressure loss is caused by friction due to the viscosity of the fluid, and the loss caused by pressure drop is known as flow resistance loss. The multi-layered annular mesh structure within the regenerator is the primary cause of flow resistance loss. Pressure drop and flow resistance loss can be calculated using semi-empirical formulas:

$$\Delta p = \frac{-2C_{ref}\mu u V}{d^2 A} \tag{15}$$

$$W_{fr} = \int_0^{2\pi}\left(\Delta p \frac{\partial V}{\partial \theta}\right)d\theta \tag{16}$$

where, C_{ref} is the Reynolds friction factor; μ is the dynamic viscosity; V is the volume of the working area; d is the hydraulic diameter; A is the flow cross-section area. The Reynolds friction factor C_{ref} is caculated as:

$$C_{ref} = \begin{cases} 16, & Re < 2000 \\ 7.343 \times 10^{-4}Re^{1.3142}, & 2000 < Re < 4000 \\ 0.7091Re^{0.75}, & Re > 4000 \end{cases} \tag{17}$$

(3)Finite speed of piston and mechanical friction loss. Relevant studies have indicated that the instantaneous pressure on the piston surface differs from the instantaneous average effective pressure within the engine cylinder[38]. The actual work of compression and expansion is different from the theoretical calculations based on classical thermodynamics. This pressure loss is caused by the finite speed motion of pressure waves generated by the piston within the working space. The formula for calculating the work loss due to finite speed of the piston and mechanical friction can be calculated as follows:

$$
\begin{aligned}
W_{FST-MF} &= \int P_m \left(\pm \frac{a u_p}{c} \pm \frac{f \Delta P_{mf}}{P_m} \right) dV \\
a &= \sqrt{3\gamma} \\
c &= \sqrt{3 R_g T}
\end{aligned}
\tag{18}
$$

where, P_m is the mean effective working pressure; u_p is the linear speed of the piston; f is the frequency; ΔP_{mf} is the pressure loss caused by mechanical friction of the components. The $\pm$ represents the compression process (+) and the expansion process (-), respectively. P_m can be calculated as :

$$
\begin{aligned}
\Delta P_{mf} &= \frac{(0.04 + 0.0045 u_p) \times 10^5}{3\mu} \left(1 - \frac{1}{r_v} \right) \\
\mu &= 1 - \frac{1}{3 r_v}
\end{aligned}
\tag{19}
$$

where, r_v is the compression ratio, $r_v = \frac{V_{max}}{V_{min}}$.

The algorithm for the model of this paper is illustrated in Fig.6. In the first step, initialize Stirling engine geometry, hydrodynamic and thermodynamic parameters. Geometric equations for V_c, V_e, dV_c and dV_e as a function of the angle of rotation are obtained from the configuration of the engine. Calculate and initialize hydrodynamic parameters such as cross-section area, wet area, hydraulic diameter, etc. based on geometric parameters. Initialize thermodynamic parameters such as specific heat capacity, gas constant and thermal conductivity;

Secondly, initialize the computational parameters. The temperatures of the expansion and compression space are initialized to the wall temperature T_{wh} and T_{wk}. The initial mass is computed by means of a first-order model;

Thirdly, initialize angle θ as 0° and set the calculation step to 1°. The angle is initialized at the end of each cycle, and for the initial value problem, the system of differential equations is solved using the fourth-order Lunge-Kutta method with θ=360° to complete the calculation of one cycle, and it is judged whether the cavity temperature at the end of the cycle is equal to the temperature at the beginning of the cycle until the gas temperature reaches the limit of convergence to turn on the next step of the calculation;

Then, calculate the regenerator's regeneration efficiency and the convection heat transfer coefficients of the heater and cooler, for details refer to literature[24]. Based on the ideal heat exchange amount obtained from the previous step, derive the actual heat exchange quantity between the heat exchanger wall and the working fluid. Compute the new temperature of the heat exchanger and use it as the initial value to return to

the third step of the ideal adiabatic model for calculation. Repeat this process until the convergence criteria are met, and then proceed to the fifth step of the calculation.

Finally, calculate the other losses to obtain the actual heat and output work. The method for solving the classical fourth-order Runge-Kutta method is shown as follows.

$$
\begin{cases}
k_1 = f\left(x_i, y_i\right) \\
k_2 = f\left(x_i + \frac{1}{2}h, y_i + \frac{1}{2}k_1\right) \\
k_3 = f\left(x_i + \frac{1}{2}h, y_i + \frac{1}{2}hk_2\right) \\
k_4 = f\left(x_i + h, y_i + hk_3\right) \\
y_{i+1} = y_i + \left[\frac{1}{6}\left(k_1 + 2k_2 + 2k_3 + k_4\right)\right] h
\end{cases}
\tag{20}
$$

D. Average pressure convergence

Here, an iterative method for pressure convergence is applied. During the process of solving the Stirling cycle, it is necessary to calculate the average pressure to meet the condition of average pressure convergence. The average pressure in the compression space over a cycle should be equal to the set average pressure, that is:

$$
\left| \int_0^\delta \left[\sum_{n=1}^{N} \frac{p_n}{N} \right] d\delta - p_{mean} \right| < p_\varepsilon p_{mean}
\tag{21}
$$

p_ε represents the residual value for determining pressure convergence. After the first cycle of the solution is completed, the initial pressure of the model is adjusted until the calculated average pressure meets the periodic stable solution as described by the above formula, that is:

$$
p_{start\_new} = p_{start\_last} - p_\varepsilon p_{start\_last}
\tag{22}
$$

Employing this iterative method allows for the rapid identification of a solution that meets the target average pressure across the entire system.

E. Verification and validation

1. Validation of the GPU-3 Engine

The GPU-3[23, 39] Stirling engine, a portable generator set developed by General Motors for the Army, has well-established equations of motion for the rhombic drive mechanism to calculate the expansion and compression space volume changes, as shown in Fig.7. The detailed design dimensions and parameters for the GPU-3 are presented in Table 2.

To validate the model, simulations (Helium, Twh = 922 K, Twk = 286 K) were carried out against the GPU-3 Stirling engine experiment with two different pressure conditions (Pmean = 2.76 MPa and Pmean = 4.14 MPa). Meanwhile, the computational results are compared with the simulation data of available second-order analysis models (Simple-II, CAFS, ISAM, Simple), the third-order analysis software Sage. The experimental data were obtained from NASA experiments on the GPU-3 Stirling engine.

Table 2. GPU-3 engine dimensions and parameters.

Parameters	Values	Parameters	Values
Clearance volumes		Swept volumes	
Compression space	28.68 cm^3	Compression space	113.14 cm^3
Expansion space	30.52 cm^3	Expansion space	120.82 cm^3
Heater		Cooler	
Tube number	40	Tube number	312
Tube inside diameter	3.02 mm	Tube inside diameter	1.08 mm
Tube length	245.3 mm	Tube length	46.1 mm
Void volume	70.38 cm^3	Void volume	13.8 cm^3
Regenerator		Drive	
Void volume	50.55 cm^3	Connecting rod length	46 mm
Length	22.6 mm	Crank radius	13.8 mm
Internal diameter	22.6 mm	Eccentricity	20.8 mm
No. per cylinder	8	Displacer stroke	31.2 mm
Diameter of wire	0.04 mm	Internal diameter of cylinder	69.9 mm
Porosity	0.697	Working fluid	Helium
Material	Stainless steel	Frequency	41.72 Hz

Table 3. RE-1000 engine dimensions and parameters.

| Parameters	Values	Parameters	Values
Heater		Cooler	
Tube number	34	Fin number	115
Void volume	27.33 cm^3	Void volume	20.43 cm^3
Regenerator		Volume	
Porosity	0.759	Expansion space	27.74 cm^3
Diameter of wire	0.0889 mm	Compression space	54.80 cm^3
Void volume	56.37 cm^3		
Displacer		Phase angle	57.5°
Stroke	24.5 mm	Frequency	30 Hz
Diameter	56.4 mm	Working fluid	Helium
Power piston		Heater temperature	873 K
Stroke	28 mm	Cooler temperature	297 K
Diameter	57.2 mm	Mean pressure	70.6 MPa
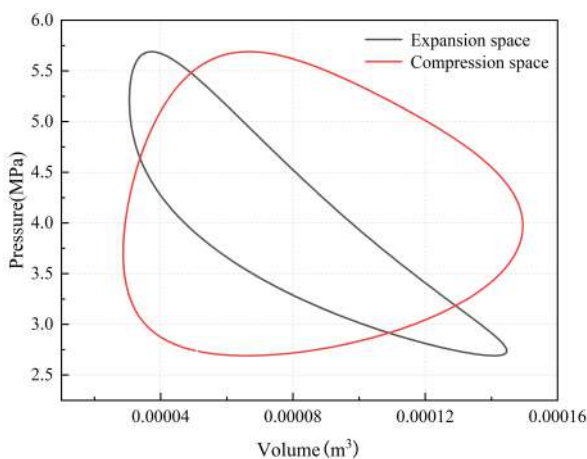
Fig. 8. Pressure–volume diagram
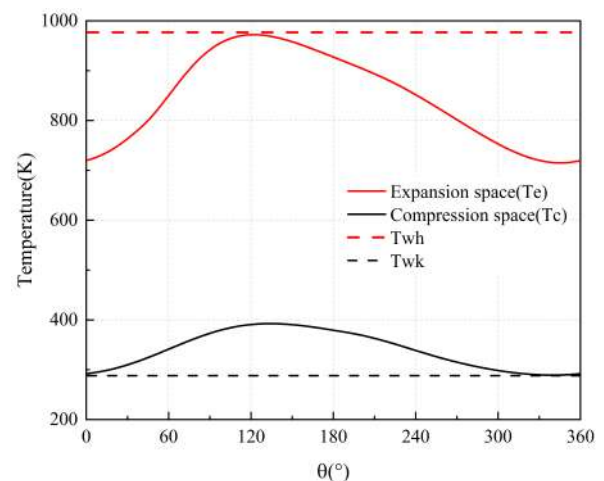
Fig. 9. Variation of the working fluid temperature

Fig.8 and Fig.9 illustrates the relationship between the working fluid temperature variation with angle in the expan-sion and compression cylinders, as well as the P-V (pressure-volume) diagram of the cycle. The temperature of the cavity
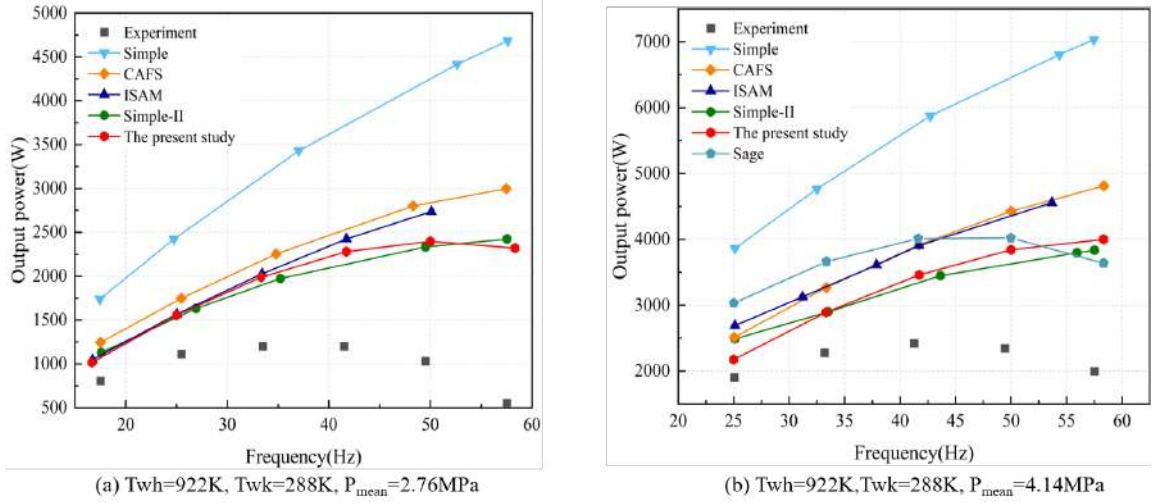
(a) Twh=922K, Twk=288K, P$_{mean}$=2.76MPa   (b) Twh=922K,Twk=288K, P$_{mean}$=4.14MPa

Fig. 10. Comparison of output power between different models and experimental values (Helium)

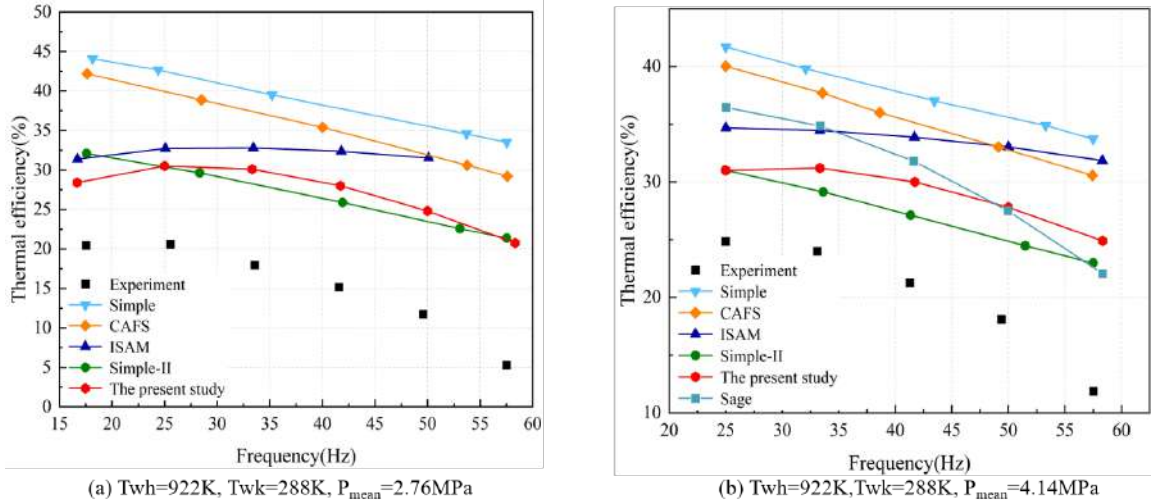(a) Twh=922K, Twk=288K, P$_{mean}$=2.76MPa   (b) Twh=922K,Twk=288K, P$_{mean}$=4.14MPa

Fig. 11. Comparison of thermal efficiency between different models and experimental values (Helium)

returns to the initial point after one complete rotation of the Stirling rhombic drive mechanism, and the cycle repeats periodically, which is in accordance with the basic characteristics of the Stirling cycle.

Fig.10 presents a comparison of the output work results between the model in this paper and the existing second-order model at various frequencies. Fig.11 displays a comparison of the cycle efficiency results between the model in this paper and the existing second-order model across different frequencies. Compared to the Simple model (Pmean=4.14 MPa), the maximum power error of this paper's model has been reduced by 152.5%, and the maximum efficiency error (as difference) has been decreased by 10.67%. The average reduction in power error across all frequency conditions is 110.0%, and the average reduction in efficiency error is 8.43%. Fig.12 illustrates the comparison of simulation values between the model in this paper and the existing second-order model under the standard operating conditions of 4.14 MPa pressure

and 41.67 Hz frequency. In comparison to the Simple model, the simulation error for output work has been lowered by 46.2%, and the simulation error (as difference) for cycle efficiency has been reduced by 8.7%. In comparison with the third-order analytical model Sage, the output work exhibited maximum and minimum errors(as difference) of 28.3% and 4.5%, respectively, with an average error of 11.5%. The cycle efficiency demonstrated maximum and minimum errors (as difference) of 5.43% and 0.30%, respectively, averaging an error of 1.55%.

Comparing the simulated and experimental values allows for the analysis of some working characteristics of the Stirling engine. When helium is used as the working fluid, the output work of the Stirling engine decreases as the frequency increases under high-frequency conditions (with a working frequency greater than 41.72 Hz), and the cycle efficiency shows an overall downward trend within the frequency analysis range we have defined, with this downward trend being
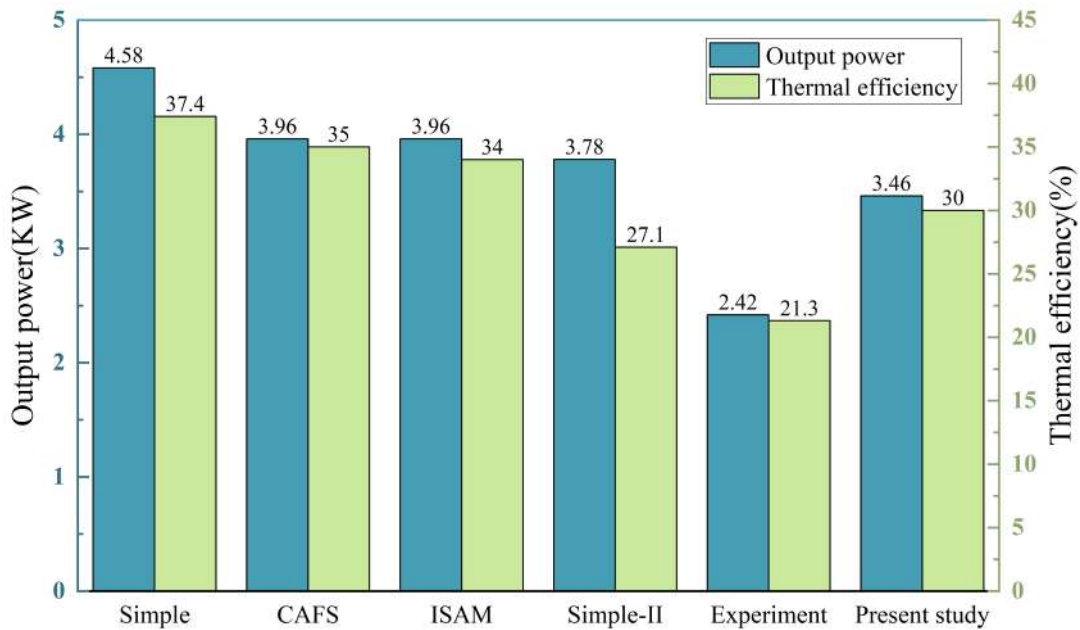
Fig. 12. Bar Chart of Simulation Results Comparison.

Table 4. Comparison of Experimental and Simulated Values of the RE-1000 engine.

Parameters	Present study	Experiment[40]
Heat in(W)	3940 (-2.4%)	4038
Indicated power(W)	1138 (10.4%)	1030
Indicated efficiency(%)	28.9 (4.4%)	25.5

particularly pronounced in the high-frequency region. On the contrary, in the subsequent parameter sensitivity analysis, it was found that when hydrogen is used as the working fluid, both the output work and cycle efficiency of the Stirling engine exhibit a significant upward trend. This difference is caused by the different material properties of the two substances. Additionally, as the working frequency increases, the error between the experimental and simulated values in the engine also gradually increases, which is due to other undetermined losses caused by high-frequency oscillating flows.

2. *Validation of the RE-1000 Engine*

In order to further validate the correctness of the model, experimental data from the RE-1000 free-piston Stirling engine, developed by NASA, was utilized for the validation process. The model was validated against the operating conditions and experimental outcomes specified in reference [40] for test case #1011. Several studies have referenced this data for the validation of the RE-1000 engine [35, 36]. The detailed design dimentions and parameters of the RE-1000 are presented in Table 3. Due to the periodic motion of the displacer and the power piston, the volume changes of the compression space and the expansion space are described as follows:

$$
\begin{aligned}
V_e &= V_{e0} - A_d X_d \sin\left(\omega t\right) \\
V_c &= V_{c0} + (A_d - A_{rod}) X_d \sin\left(\omega t\right) \\
&\quad - A_p X_p \sin\left(\omega t - \alpha\right)
\end{aligned}
\tag{23}
$$

where, the terms V_e and V_c denote the initial volumes of the expansion and compression spaces, respectively, at the equilibrium positions of the displacer and the power piston; A_d, A_p and A_{rod} represent the cross-sectional areas of the displacer, power piston, and connecting rod, respectively; X_d and X_p are the displacer amplitude and power piston amplitude; α is the angular difference between the motions of the displacer piston and the power piston. It is used to describe the synchronization between the pistons' movements and can impact the efficiency and power output of the engine.

Table 4 shows the results of the comparison between experimental and simulated values. The relative errors for the input heat, output work, and cycle efficiency are correspondingly -2.4%, 10.4%, and 4.4%. The validation against experimental and simulated data from the GPU-3 and RE-1000 Stirling engines has demonstrated the model's high level of precision.
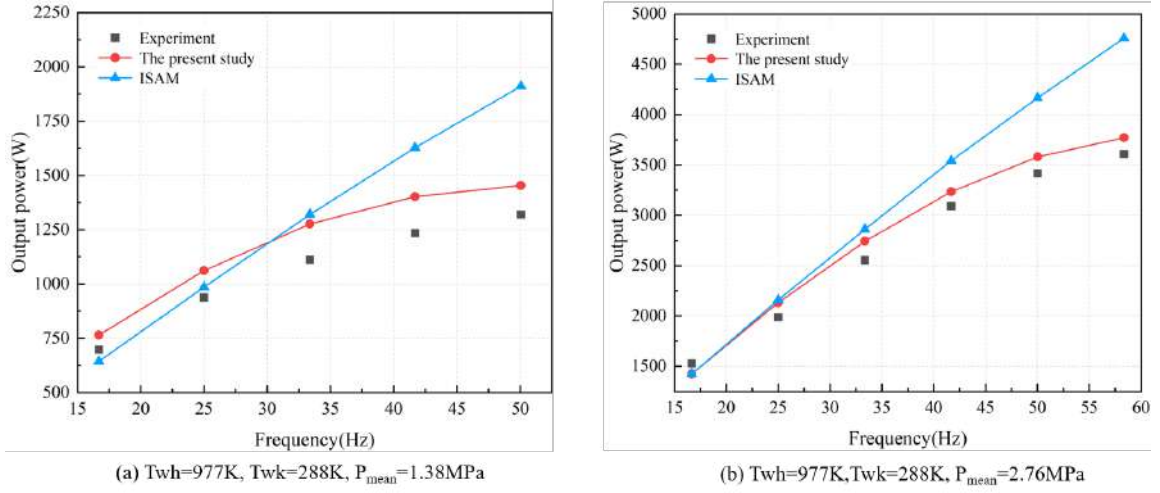
(a) Twh=977K, Twk=288K, P_{mean}=1.38MPa

(b) Twh=977K, Twk=288K, P_{mean}=2.76MPa

Fig. 13. The variation of output power with frequency (Hydrogen)

(a) Twh=977K, Twk=288K, P_{mean}=1.38MPa
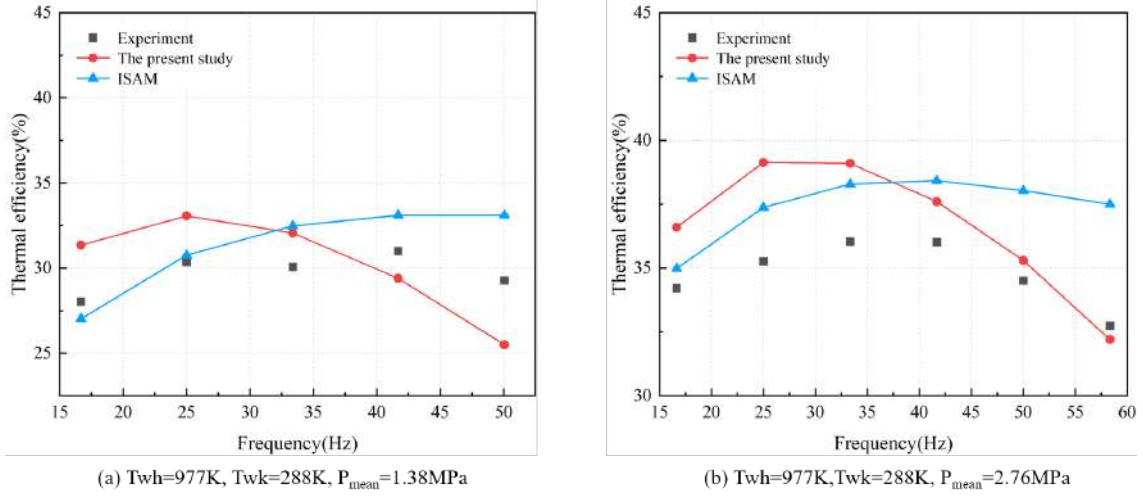
(b) Twh=977K, Twk=288K, P_{mean}=2.76MPa

Fig. 14. The variation of efficiency with frequency (Hydrogen)

IV. PARAMETER SENSITIVITY ANALYSIS

A. Effect of frequency and different working fluids

The selection of working fluids for Stirling engines is predominantly focused on gases, with commonly used working fluids being N_2, H_2, CO_2, He, and air. Due to the superior heat exchange characteristics of small molecular weight gases, most technologically advanced high-power Stirling engines employ He or H_2 as their working fluids.

In order to investigate the effects of frequency and different work materials on the output work and cycle efficiency, hydrogen is selected as the work material (Twh=977 K, Twk=288 K), with two different pressure variables set at 1.38 MPa and 2.76 MPa. Fig.13a and Fig.13b give the changes of the output work with the frequency. Fig.14a and Fig.14b give the changes of the cycle efficiency with the frequency.
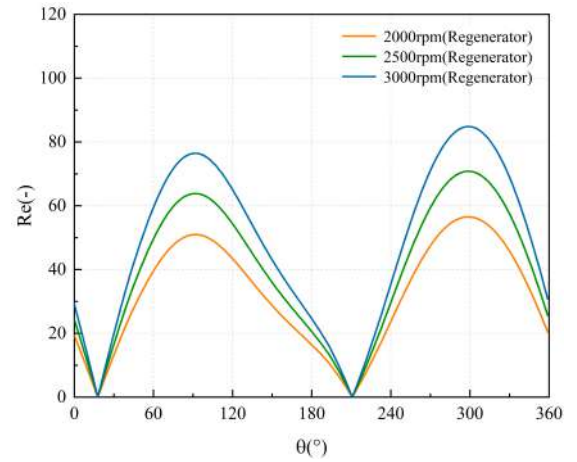

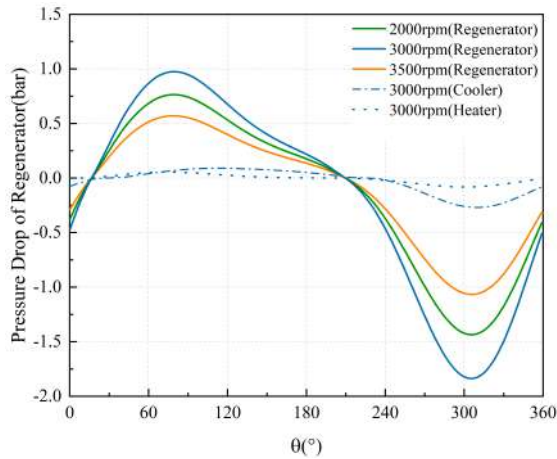Fig. 15. Effect of rotation speed on Reynolds number of regenerator

Fig. 16. Effect of rotation speed on pressure drop of regenerator
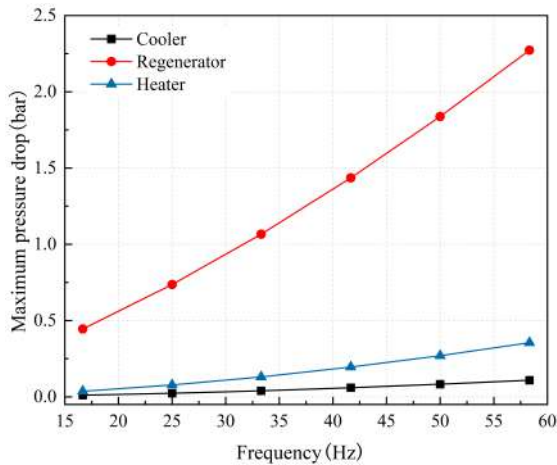

Fig. 17. The maximum pressure drop of the heat exchanger varies with frequency

In scenarios of slower rotation, the efficiency of the system increases with increased rotation speed. However, as the speed of rotation continues to rise, there is a decrease in system efficiency, resulting in a general trend of initial increase followed by a decrease. When the work material is H_2, there is a clear rise in the power output of the Stirling engine with the increase in rotational speed, and the upward trend is sharp. On the other hand, when the work material is He, the faster rotation speed clearly has a detrimental impact on the Stirling engine's output, with a less steep upward trend. Given that the regenerator embodies a screen-like structure, a substantial pressure drop transpires as the working mass flows through it, consequently yielding a loss attributed to flow resistance. Fig.15 and Fig.15 demonstrates the effect of different rotation speeds on the pressure loss and Reynolds number of regenerator. Fig.17 demonstrates the variation of the maximum pressure drop within the heat exchanger with frequency. With the increase in frequency, the Reynolds number and pressure loss inside the heat exchanger both increase. Compared to the pressure loss in the regenerator, the pres-

sure losses in the cooler and heater are negligible, confirming that the wire mesh structure of the regenerator is the primary source of pressure loss. The high rotational speed of the Stirling engine makes the oscillating flow and heat exchange of the work material inside the body tend to be complicated, resulting in a significant increase in the flow resistance loss or local loss, which in turn affects the cycle efficiency. H_2 possessing a lower dynamic viscosity coefficient, produces relatively smaller flow resistance loss when operating at high rotational speeds than He. However, H_2 exhibits poor sealing properties, making it prone to leakage and explosion, and it can cause issues such as hydrogen embrittlement in certain materials. Therefore, helium is commonly chosen as the working fluid.

B. Effect of regenerator parameters

The regenerator features an internal structure filled with a metal wire mesh. Porosity is represented by the ratio of the regenerator's porous volume to its overall volume. Fig.18 depicts the variation of output work and cyclic efficiency with changes in porosity and wire mesh diameter. For metal wire meshes of different diameters, the cyclic efficiency tends to increase initially and then decrease. This trend is attributed to the fact that an appropriate increase in porosity enlarges the hydraulic diameter and reduces the wetted area of the mesh in contact with the working fluid. This reduction in pressure drop across the regenerator leads to a decrease in flow resistance losses, thereby enhancing the output work and cyclic efficiency of the engine. At lower porosities, a denser mesh configuration results in a smaller hydraulic diameter and an increased wetted area for the regenerator, which can significantly impact the flow resistance and adversely affect the cyclic efficiency and output work.

When the porosity is below 0.797, Stirling engines equipped with larger diameter wire meshes have higher cyclic efficiencies compared to those with smaller diameter meshes. This is due to the larger convective heat transfer area provided by the larger diameter meshes under conditions of low porosity. On the contrary, when the porosity surpasses 0.797, wire meshes of a smaller diameter demonstrate superior cyclic efficiencies, attributable to their comparatively lesser flow resistance losses. At a wire mesh diameter of 0.04 mm, a turning point in cyclic efficiency is observed at a porosity of 0.797. With the further escalation of porosity to 0.847, there is a slight rise of 0.1% in output power, while the cyclic efficiency drops by 3%. In conclusion, the engine's output work and cyclic efficiency are most optimal at a porosity of 0.797.

Fig.19 illustrates the variation of output work and cycle efficiency with the length of the regenerator. It can be observed from the figure that at a mean pressure of 4.14 MPa, an inflection point appears in the cycle efficiency curve when the regenerator length is around 0.025 meters. When the regenerator length is less than 0.025 meters, an increase in length leads to a larger heat exchange area, allowing for more sufficient heat transfer within the regenerator's metal wire mesh, which in turn increases cycle efficiency with the increase in
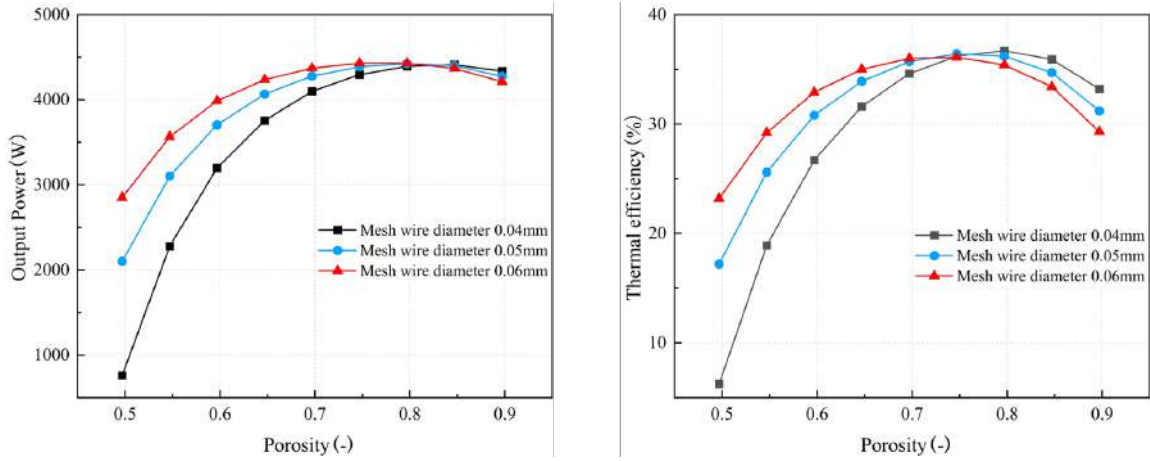
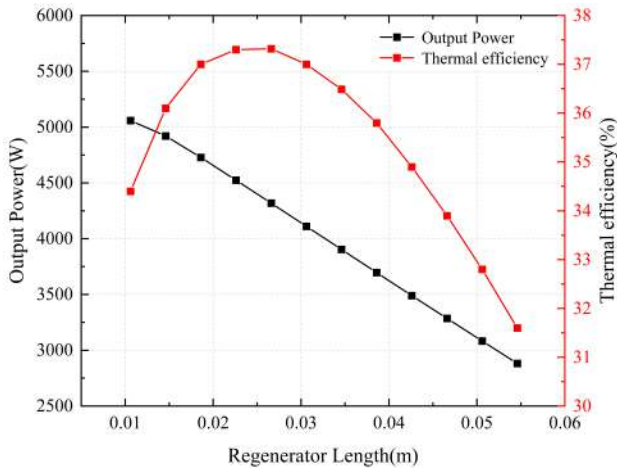Fig. 18. The influence of the porosity and wire diameter

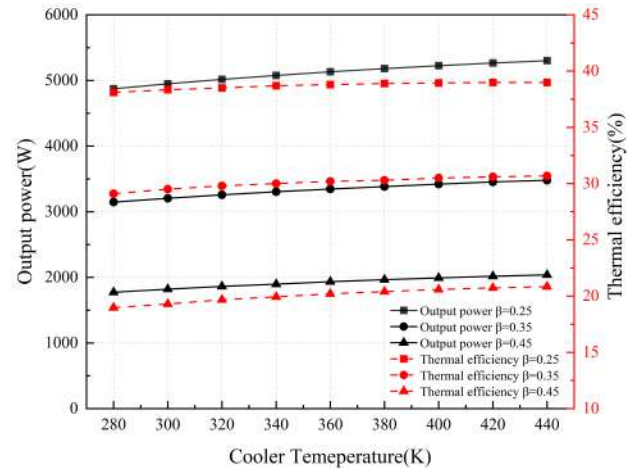Fig. 19. The influence of the regenerator length

Fig. 20. The influence of the temperature ratio

length. Moreover, since the pressure losses due to flow resistance will inevitably increase with length, the output work will necessarily decrease as the regenerator lengthens. This creates a situation where, when the regenerator length exceeds 0.025 meters, the positive effect of increased heat exchange area on cycle efficiency is not sufficient to offset the negative effect caused by increased losses, resulting in a decline in cycle efficiency. It can be observed that under the condition of Pmean=4.14 MPa, the optimal regenerator length is around 0.025 m.

C. Effect of temperature of heat exchangers

In the actual operation of a space nuclear reactor, the hot-end temperature of a Stirling system fluctuate with alterations in the core temperature of the nuclear reactor, and the performance of the radiative heat rejection system can also affect the cold-end temperature. Shifts in both the hot-end and cold-end temperatures directly impact the quantity of heat

absorbed and released by the working fluid gas, thereby influencing the output work and cyclic efficiency of the Stirling engine. Consequently, with respect to the space nuclear power reactor, it is necessary to assess the impact of cold-end and hot-end temperatures on the performance of the Stirling system.

Fig.20 demonstrates the variation in output work and cyclic efficiency of the Stirling engine at different temperature ratio conditions as the cooler temperature increases from 280 K by increments of 20 K up to 440 K. At a temperature ratio of 0.25, the output work increases from 4874 W to 5301 W, marking an increment of 2.3%. At a temperature ratio of 0.35, the output work rises from 3146 W to 3480 W, an increase of 5.4%. When the temperature ratio is 0.45, the output work surges from 1773 W to 2037 W, denoting an increase of 9.8%. When the temperature ratio is fixed, alterations in the cooler temperature negligibly influence the output work and cyclic efficiency. In actual scenarios, due to material constraints, the heater of a Stirling engine cannot reach excessively high temperatures, so the ideal case is considered here. With a

constant cooler temperature, when the temperature ratio increases from 0.25 to 0.35, the output work decreases on average by 34.8%, and the cyclic efficiency decreases by 8.61% on average. When the temperature ratio increases from 0.35 to 0.45, the output work decreases on average by 42.3%, and the cyclic efficiency decreases by an average of 10.0%. It can be observed that the lower the temperature ratio, the higher the system's output power and cyclic efficiency. Conversely, the higher the temperature ratio, the lower the system's output power and cyclic efficiency. With a constant cooler temperature, a higher heater temperature is more conducive to achieving satisfactory output work and cyclic efficiency. Similarly, under the condition of constant heater temperature, the lower the cooler temperature, the better the engine performance. However, in practice, due to the impact of environmental factors, the cooler cannot achieve excessively low temperatures, and this should be taken into account based on actual conditions. The operating temperature of the working fluid in high-temperature heat pipes exceeds 730K. Among them, the most frequently used sodium heat pipes have a working temperature range of 700-1100K. The hot end of the Stirling engine transfers heat to the high-temperature heat pipe through solid-to-solid contact, while the cold end can only dissipate heat into the space environment through radiative cooling. Therefore, for space power devices, thermal efficiency is particularly important; a higher thermal efficiency means that under the same weight and cost conditions, it allows for a higher power output or a longer operational time.

In the parameter sensitivity analysis of the cold and hot end temperatures, we have fixed the temperature boundaries to simulate the operating conditions under steady-state. However, in practical engineering applications, temperature control and thermal management are typically complex and critical issues. For example, during the reactor start-up process, there is a significant concern about controlling the thermal balance throughout the entire process, from the heat generated in the core to its transfer via high-temperature heat pipes to the Stirling engine and finally to the heat rejection system. Heat pipes are often quite fragile, and initiating a cold start of the Stirling engine could lead to thermal imbalance, causing the heat pipes to fail and posing a risk to the safety of the reactor. Therefore, for the start-up issue, it is necessary to devise a reasonable temperature control plan to balance the heat transfer between various components. We will explore this issue in subsequent work.

V. CONCLUSION

Stirling engines, with their high efficiency, strong reliability, and compact structure, have attracted significant attention from researchers, especially in recent decades, leading to substantial development and an irreplaceable role in various fields. To investigate the operational characteristics of Stirling engines, this paper establishes a second-order analysis model, thoroughly validates it, and conducts extensive parameter analysis based on the validated model. The specific work includes:

(1) The model developed in this paper is fully validated against the experimental data of the GPU-3 Stirling engine from NASA. Under the condition of 4.14 MPa pressure, compared to the Simple model, the maximum power error has been reduced by 152.5%, and the maximum efficiency error has been lowered by 10.67%. The average reduction in power error across all frequency conditions is 110.0%, and the average reduction in efficiency error is 8.43%. Furthermore, comparisons were also conducted with the experimental data of the RE-1000 free-piston Stirling engine. The results show that the model developed in this paper demonstrates equivalent accuracy compared with existing second-order models, thereby confirming the correctness of the model.

(2) This study investigates the impact of working fluids on the operational characteristics of Stirling engines. The results indicate that hydrogen, with its low dynamic viscosity coefficient and reduced flow resistance losses, can generate higher output power when used as the working fluid in Stirling engines. Additionally, the research reveals that high rotational speeds lead to complex oscillatory flow phenomena, resulting in increased pressure drops. Furthermore, as the Reynolds number increases, flow resistance losses rise, leading to a reduction in the engine's output power.

(3) The output power and cycle efficiency of the Stirling cycle were simulated under different wire mesh porosities and diameters. The results showed porosity, wire diameter, and regenerator length all have a significant impact on the performance of the Stirling engine. When the wire mesh diameter is 0.04 mm, the optimal porosity is 0.797, and the optimal regenerator length is around 0.025 m.

(4) The performance of a Stirling engine in a space nuclear reactor is significantly influenced by the hot-end and cold-end temperatures. Variations in these temperatures directly affect the heat exchange and efficiency of the engine. Optimal temperature ratios enhance output work and efficiency, while extremes can lead to significant reductions. Thermal management, particularly during start-up, is critical to prevent thermal imbalance and ensure reactor safety. .

VI. FUNDING

[1] G. L. Bennett, Space nuclear power: opening the final frontier. Paper presented at the 4th International Energy Conversion Engineering Conference and Exhibit (IECEC), San Diego, Cali-

fornia, 4191 (2006). DOI:10.2514/6.2006-4191

[2] R. A. Johnson, W. T. Morgan, S. R. Rocklin, Design, ground test and flight test of SNAP 10A, first reactor in space. NUCL. ENG. DES, **5** (1), 7-21 (1967). DOI:10.1016/0029-5493(67)90074-X

[3] M. S. El-Genk, Deployment history and design considerations for space reactor power systems. ACTA. ASTRONAUT, 64 (9-10), 833-849 (2009). DOI:10.1016/j.actaastro.2008.12.016

[4] E. Cliquet, J. M. Ruault, J. P. Roux, et al, Study of Space Reactors for Exploration Missions. Paper presented at Proceedings of the 4th European Conference for Aerospace Sciences (EUCASS), Saint Petersburg, Russia, 168 (2011).

[5] L. S. Mason, A comparison of Brayton and Stirling space nuclear power systems for power levels from 1 kilowatt to 10 megawatts. Amer. Inst. Phys, **552** (1), 1017-1022 (2001). DOI:10.1063/1.1358045

[6] H. X. Yu, Y. G Ma, Z. H. Zhang, et al Initiation and development of heat pipe cooled reactor. Nucl. Power. Eng, **40** (4), 1-8 (2019). (in Chinese) DOI: 10.13832/j.jnpe.2019.04.0001

[7] B. H. Yan, C. Wang, L. G. Li, The technology of micro heat pipe cooled reactor: A review. Ann. Nucl. Energy, **135**, 106948 (2020). DOI: 10.1016/j.anucene.2019.106948

[8] Y. G. Ma, E. H. Chen. H. X. Yu, R. C. Zhong, et al, Heat pipe failure accident analysis in megawatt heat pipe cooled reactor. Ann. Nucl. Energy, **149**, 107755 (2020). DOI: 10.1016/j.anucene.2020.107755

[9] Y. G. Ma, W. B. Han, B. H. Xie, Coupled neutronic, thermal-mechanical and heat pipe analysis of a heat pipe cooled reactor. Nucl. Eng. Des, **384**, 111473 (2021). DOI: 10.1016/j.nucengdes.2021.111473

[10] Z. P. Zhang, C. L. Wang, K. L. Guo, et al, Steady-state multi-physics coupling analysis of heat pipe cooled reactor core. Prog. Nucl. Energ, **165**, 104901 (2023). DOI: 10.1016/j.pnucene.2023.104901

[11] Z. X. Tian, C. L. Wang, K. L. Guo, et al, A review of liquid metal high temperature heat pipes: Theoretical model, design, and application. Int. J. Heat. Mass. TRAN, **214**, 124434 (2023). DOI: 10.1016/j.ijheatmasstransfer.2023.124434

[12] R. Stirling, Stirling air engine and the heat regenerator. US Patent, 4081, 16 (1816).

[13] Z. W. Dai, C. L. Wang, D. L. Zhang, et al, Design and analysis of a free-piston stirling engine for space nuclear power reactor. Nucl. Eng. Technol, **53** (2), 637-646 (2021). DOI: 10.1016/j.net.2020.07.011

[14] Z. W. Dai, C. L. Wang, D. L. Zhang, et al, Design and heat transfer optimization of a 1 kW free-piston stirling engine for space reactor power system. Nucl. Eng. Technol, **53** (7), 2184-2194 (2021). DOI: 10.1016/j.net.2021.01.022

[15] C. H. Yang, N. L. Zhuang, H. B. Zhao, et al, Dynamic performance of the combined stirling thermoelectric conversion technology for a lunar surface nuclear power system. Appl. Therm. Eng, **221**, 119873 (2023). DOI: 10.1016/j.applthermaleng.2022.119873

[16] J. Zhao, C. L. Wang, X. Liu, et al, Operation and safety analysis of space lithium-cooled fast nuclear reactor. Ann. Nucl. Energy, **166**, 108729 (2022). DOI: 10.1016/j.anucene.2021.108729

[17] C. H. Yang, N. L. Zhuang, W. A. Du, et al, Modified Stirling cycle thermodynamic model IPD-MSM and its application. Energ. Convers. Manage, **260**, 115630 (2022). DOI: 10.1016/j.enconman.2022.115630

[18] D. I. Poston, The heatpipe-operated Mars exploration reactor (HOMER). Appl. Int. Forum, **552** (1), 797-804 (2001). DOI: 10.1063/1.1358010

[19] M. A. Gibson, S. R. Steven, I. David, NASA's Kilopower reactor development and the path to higher power missions. 2017 IEEE aerospace conference, 1-14 (2017). DOI: 10.1109/AERO.2017.7943946

[20] H. L. Chen, W. X. Wang, A. G. Wu, et al, Multi-physics coupling analysis of test heat pipe reactor KRUSTY based on MOOSE framework. Nucl. Eng. Des, **414**, 112597 (2023). DOI: 10.1016/j.nucengdes.2023.112597

[21] Z. A. Guo, L. M. Liu, Z, Y, Liu, et al, Development and application of a transient analysis code for heat pipe cooled reactor systems. Nucl. Eng. Des, **419**, 112979 (2024). DOI: 10.1016/j.nucengdes.2024.112979

[22] M. A. Gibson, D. I. Poston, P. M. McClure, The Kilopower Reactor Using Stirling TechnologY (KRUSTY) nuclear ground test results and lessons learned. 2018 International Energy Conversion Engineering Conference, 4973 (2018). DOI: 10.2514/6.2018-4973

[23] W. R. Martini, Stirling engine design Manual. NASA CR-135382. (1978).

[24] I. Urieli, D. Berchowitz, Stirling cycle engine analysis. Bristol: Adam Hilger. (1984).

[25] M. Babaelahi, H. Sayyaadi, Simple-II: a new numerical thermal model for predicting thermal performance of Stirling engines. Energy, **69**, 873-890 (2014).DOI: 10.1016/j.energy.2014.03.084

[26] H. Hosseinzade, H. Sayyaadi, CAFS: The Combined Adiabatic–Finite Speed thermal model for simulation and optimization of Stirling engines. Energ. Convers. Manage, **91**, 32-53 (2015).DOI: 10.1016/j.enconman.2014.11.049

[27] M. J. Ni, B. W. Shi, G. Xiao, Improved Simple Analytical Model and experimental study of a 100 W β-type Stirling engine. Appl. Energ, **91**, 32-53 (2015). DOI: 10.1016/j.apenergy.2016.02.069

[28] K. Wang, S. Dubey , F. H. Choo, et al, A transient one-dimensional numerical model for kinetic Stirling engine. Appl. Energ, **183**, 775-790 (2016). DOI: 10.1016/j.apenergy.2016.09.024

[29] H. Qiu, K. Wang, P. F. Yu, et al, A third-order numerical model and transient characterization of a β-type Stirling engine. Energy, **222**, 119973 (2021). DOI: 10.1016/j.energy.2021.119973

[30] G. Xiao, Y. Q. Huang, S. L. Wang, et al, An approach to combine the second-order and third-order analysis methods for optimization of a Stirling engine. Energ. Convers. Manage, **165**, 447-458 (2018). DOI: 10.1016/j.enconman.2018.03.082

[31] J. L. Salazar, W. L. Chen, A computational fluid dynamics study on the heat transfer characteristics of the working cycle of a β-type Stirling engine. Energ. Convers. Manage, **88**, 177-188 (2014). DOI: 10.1016/j.enconman.2014.08.040

[32] M. A. Mohammadi, A. Jafarian, CFD simulation to investigate hydrodynamics of oscillating flow in a beta-type Stirling engine. Energy, **153**, 287-300 (2018). DOI: 10.1016/j.energy.2018.04.017

[33] W. D. Zhao, R. J. Li, H. L. Li, et al, Numerical analysis of fluid dynamics and thermodynamics in a Stirling engine. Appl. Therm. Eng, **189**, 116727 (2021). DOI: 10.1016/j.applthermaleng.2021.116727

[34] K. L. Lee, C. Tarau, W. G. Anderson, et al, Titanium-water heat pipe radiators for space fission power system thermal management. Energy, **33** (7), 1100-1114 (2008). DOI: 10.1007/s12217-020-09780-5

[35] D. J. Kim, Y. C. Park, K. Sim, Development and validation of an improved quasisteady flow model with additional parasitic

loss effects for Stirling engines. INT. J. ENERG. RES, **2024** (1), 8896185 (2024). DOI: 10.1155/2024/8896185

[36] F. Formosa, Coupled thermodynamic–dynamic semi-analytical model of free piston Stirling engines. Energ. Convers. Manage, **52** (5), 2098-2109 (2011). DOI: 10.1016/j.enconman.2010.12.014

[37] Y. Timoumi, I. Tlili, S. B. Nasrallah, Design and performance optimization of GPU-3 Stirling engines. Energy, **33** (7), 1100-1114 (2008). DOI: 10.1016/j.energy.2008.02.005

[38] S. Petrescu, C. Dobre, C. Stanciu, et al, The Direct Method from Thermodynamics with Finite Speed used for Performance Computation of quasi-Carnot Irreversible Cycles. Rev. Chim-Bucharest, **63**, 74-81 (2012).

[39] F. Ahmed, H. L. Huang, S. Ahmed, et al, A comprehensive review on modeling and performance optimization of Stirling engine. INT. J. ENERG. RES, **44** (8), 6098-6127 (2020). DOI: 10.1002/er.5214

[40] J. G. Schreiber, S. M. Geng, G. V. Lorenz, RE-1000 free-piston Stirling engine sensitivity test results. National Aeronautics and Space Administration Report 1. (1986).